Emergent topological properties in spatially modulated sub-wavelength-barrier lattices

Giedrius Žlabys,[1,*] Wen-Bin He,[1] Domantas Burba,[2] Sarika Sasidharan Nair,[1] Thomas Busch,[1,†] and Tomoki Ozawa[3]

[1]*Quantum Systems Unit, Okinawa Institute of Science and Technology Graduate University, 904-0495 Okinawa, Japan*
[2]*Institute of Theoretical Physics and Astronomy, Faculty of Physics, Vilnius University, Saulėtekio 3, LT-10257 Vilnius, Lithuania*
[3]*Advanced Institute for Materials Research (WPI-AIMR), Tohoku University, Sendai 980-8577, Japan*

(Received 22 December 2025; accepted 2 March 2026; published 1 April 2026)

We investigate topological phenomena in a spatially modulated Dirac-δ lattice, where the scattering potential varies periodically in space. Changing the potential modulation frequency leads to Hofstadter's butterfly-like energy spectrum and enables the emergence of topological transport regimes characterized by nontrivial Chern numbers. We show how the considered modulated system is connected to the Hofstadter model via the Harper equation. By adiabatically varying spatial modulation parameters, we demonstrate controllable quantum transport and verify the topological nature of these effects through Wannier center displacement and bulk invariant calculations. We also propose an experimentally feasible realization of such a system using optically controlled three-level atoms. Our findings showcase spatially engineered Kronig–Penney-type systems as versatile platforms for investigating and exploiting different topological quantum transport regimes.

DOI: 10.1103/gf47-yh4z

I. INTRODUCTION

The Kronig–Penney model provides a paradigmatic description of crystalline solids with periodic potentials [1]. It is a one-dimensional continuum model in which a particle moves in a periodic array of short-range scatterers, often represented by a Dirac comb potential. It serves as an analytically tractable minimal description of low-dimensional condensed-matter materials, capturing the physics of transport [2], localization, and disorder [3–5]. Recent theoretical and experimental developments in ultracold atomic systems allow such toy models to be realized in precisely controllable environments, with individually tunable positions and scattering strengths of the potential barriers. Ultracold atomic systems offer a versatile platform where potentials with subwavelength structure can be engineered by using the spatial dependence of the nonlinear atomic response associated with the dark state of a three-level system [6–10], Fourier-synthesis of lattices utilizing multiphoton Raman transitions [11], optical or radio-frequency dressing of optical potentials [12], and trapping in near-field guided modes with nanophotonic systems [13]. These potentials are also supported by photonic crystals [14,15].

A central theme driving much of modern condensed-matter physics is the profound role of topology. The discovery of the quantum Hall effect revealed that quantum states could possess global properties, characterized by topological invariants, leading to robust phenomena such as quantized conductance immune to local perturbations [16]. Thouless pumping emerged as a powerful concept connecting the static topological properties with dynamic response [17]. It demonstrated that the adiabatic and periodic change of system parameters could induce quantized transport, directly related to a topological invariant known as the Chern number. This provided another experimental avenue for probing topology [18,19]. Crucially, Thouless pumping allows us to access high-dimensional systems by interpreting periodically varying parameters as synthetic dimensions. Thus, topological phenomena governed by Chern numbers can be engineered and studied even in systems that are effectively one-dimensional [20–23].

Kronig–Penney-type models naturally lend themselves to such topological engineering. Parameters controlling modulation of the barrier positions or strengths can be mapped to synthetic dimensions, realizing effective higher-dimensional band structures with nontrivial topology. Moreover, these systems have been shown to support topological edge states [24–27], demonstrating that nontrivial topology can be implemented and controlled at the level of continuum scattering potentials. The combination of analytical tractability, flexible tunability, and experimental accessibility therefore makes Kronig–Penney-type models an ideal setting to investigate topological transport.

In this work, we investigate the topological properties arising in a spatially modulated Dirac-δ lattice, where the scattering strengths of the equidistantly placed δ-function potentials vary periodically in space. Specifically, we show that changing the frequency of this spatial modulation leads to the emergence of Hofstadter-like energy spectra, reminiscent

*Contact author: giedrius.zlabys@oist.jp
†Contact author: thomas.busch@oist.jp

of electrons in a two-dimensional lattice under a magnetic field. We demonstrate that this spatial modulation, coupled to the adiabatic variation of the modulation parameters, enables control over quantum transport due to the presence of nontrivial topology in the system. We explicitly calculate the Chern numbers of the spectrum, illustrating various possible transport regimes depending on the filling of the energy bands. To solidify the connection to established topological frameworks, we compute the Wannier center displacement using different pumping protocols, confirming that they match the results obtained from the bulk topological invariant calculations and highlighting the role of the spatial barrier modulation as an effective magnetic flux that controls the periodicity length scale. Finally, we propose how to implement such a periodically modulated sub-wavelength-barrier system in an experimentally accessible three-level dark state lattice. Our work reveals how spatially structured potentials in simple lattice models can serve as a resource for engineering topological states and controlling quantum dynamics.

II. MODEL

We consider a one-dimensional system of equidistantly spaced Dirac-δ scatterers (barriers) with spatially cosine-modulated scattering amplitudes (heights). It is described by the dimensionless Hamiltonian

$$H = -\frac{\mathrm{d}^2}{\mathrm{d}x^2} + \sum_{j\in\mathcal{M}} h_j^{\alpha\beta\gamma\Delta}\delta\big(x - x_j^{\Delta}\big), \tag{1}$$

where

$$h_j^{\alpha\beta\gamma\Delta} \equiv h_0\big[1 + \alpha\cos\big(2\pi\beta x_j^{\Delta} - \gamma\big)\big]. \tag{2}$$

Throughout the paper, energy is taken to be dimensionless and is measured in terms of $E_0 = \hbar^2/2ma^2$, where a is the separation between neighboring barriers, m is the mass of the particle, and $\hbar$ is the reduced Planck's constant. The position coordinate x and the jth barrier position $x_j^{\Delta} = x_j + \Delta$ are measured in units of a, where $x_j \equiv x_j^0$ and for numerical calculations we set $x_0 = 0$. $\mathcal{M} \subset \mathbb{Z}$ is the indexing set of the barriers and the parameter Δ indicates a global translation of all of the scatterers by distance Δ under the height modulation function. The cosine modulation amplitude is $\alpha \in [0, 1]$, and its spatial frequency and phase are β and $\gamma \in [0, 2\pi)$ (a shift of $\gamma = 2\pi\beta$ is equivalent to translating the whole lattice by scatterer separation distance a). When the modulation is turned off ($\alpha = 0$), the height of all barriers is h_0. An example spatial barrier configuration for $\beta = 1/5$ is shown in Fig. 1(a) for two elementary cells of length b. The evolution of the barrier positions and heights under periodic change of γ and Δ are shown in Figs. 1(b) and 1(c), respectively.

III. RESULTS

A. Band structure

One of the key properties required for topological transport is the presence of isolated bands throughout the entire variable parameter regime, i.e., throughout the range of γ and Δ. To determine their existence, controllability, and to identify their bounds, we first calculate the energy-band structure of the system.

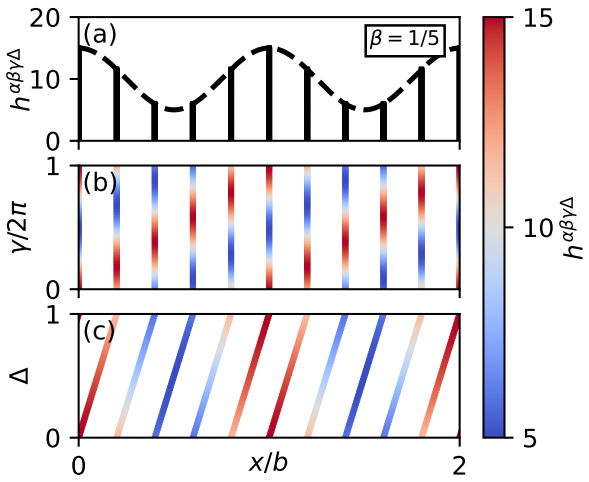

FIG. 1. (a) Equidistantly spaced sub-wavelength barriers with scattering amplitudes $h^{\alpha\beta\gamma\Delta}$ for modulation parameters $\beta = 1/5$, $\Delta = 0, \gamma = 0, h_0 = 10$, and $\alpha = 0.5$. The black dashed line indicates the modulation envelope. (b) Evolution of the barrier heights $h^{\alpha\beta\gamma\Delta}$ as γ is changed while $\Delta = 0$. (c) Evolution of the barrier heights and positions as Δ is changed while $\gamma = 0$.

The energy bands of the model are obtained by imposing a periodic boundary condition (PBC) for the coordinate x and solving the eigenvalue problem in quasimomentum k space (see Appendix A). The system satisfies PBC only if β is rational. For numerical calculations, we select $\beta = p/q$ with $q \in \{2, 3, \ldots, 30\}$ and p being all coprimes of q such that $0 < \beta < 1$.

We first calculate the set of energy eigenvalues $E(k, \gamma, \beta)$ and look at the band structure as a function of modulation frequency β, for all values of k and γ while $\Delta = 0$. The topological properties of the system will depend only on the presence of band gaps throughout the parameter domain; therefore, the relevant information is encoded in the projected bands $E(\beta) = \{E(k, \gamma, \beta)|k \in (-\pi/b, \pi/b], \gamma \in [0, 2\pi)\}$ for each β. It is important to note that $E(k, \Delta, \beta)$ for $\gamma = 0$ shares the same projected band structure $E(\beta) = \{E(k, \Delta, \beta)|k \in (-\pi/b, \pi/b], \Delta \in [0, 1)\}$, since varying either Δ or γ periodically covers the whole barrier configuration space, albeit in a different manner, leading to the same gap structure. The lowest projected energy band for different modulation strengths α is shown in Figs. 2(a)–2(e). We see that, as α increases, the band splits into sub-bands forming a Hofstadter's butterfly-like spectrum [28]. In this sense, α plays a role analogous to the hopping anisotropy ratio in the Hofstadter model, where gap formation emerges as the ratio approaches unity [29]. The higher energy bands behave in a similar fashion (see Appendix A). The number of sub-bands in each band is numerically observed to be q. In the even-q case, the $q/2$ and $q/2 + 1$ sub-bands touch at energies $E_{K_n}^{\mathrm{mid}} = K_n^2$ where K_n are the solutions of the equation $\frac{h_0}{2K_n}\sin(K_n) + \cos(K_n) = 0$ with ordering $0 \leqslant K_1 < K_2 < \cdots < K_n$. These are the eigenenergies of the system at $k = \pm\pi/2$ when all barrier heights are equal, thus they do not depend on α and the wave functions form standing waves (see Appendix B).

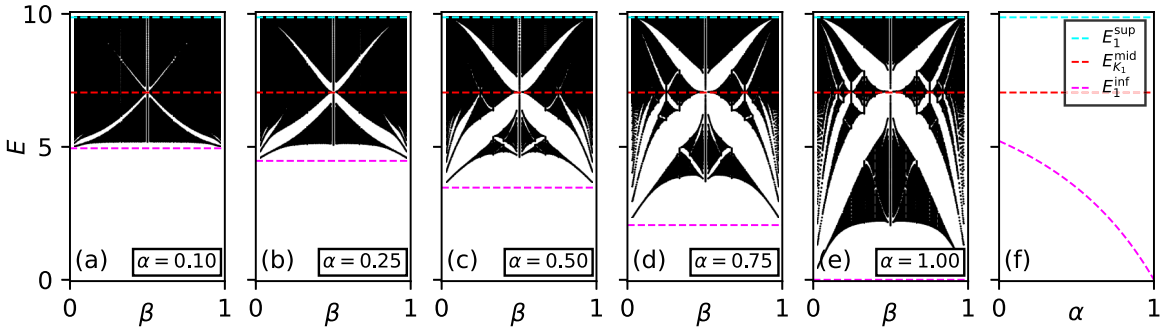

FIG. 2. Emergence of the butterfly-like energy spectrum in the lowest projected energy band $E(\beta)$ as the modulation amplitude α is increased. Panels (a)–(e) correspond to $\alpha = 0.1,\ 0.25,\ 0.5,\ 0.75$, and 1. The energies of the upper bound E_1^{sup}, standing-wave solution $E_{K_1}^{\mathrm{mid}}$, and the lower bound E_1^{inf} are indicated by cyan, red, and magenta dashed lines, respectively, and their dependence on α is shown in panel (f). The unmodulated height is fixed at $h_0 = 10$.

Each of the energy bands, independently of h_0, α, and β, is bounded from above by $E_n^{\mathrm{sup}} = (\pi n)^2,\ n \in \mathbb{N}$, where n is the energy band index. This corresponds to the case when the eigenstates of the system effectively do not feel the Dirac-δ potential since the zeros of the wave functions coincide with the positions of the barriers. Thus, only the kinetic-energy contribution is present.

Finally, the lower energy bound E_1^{inf} of the spectrum is determined by solving the standard Kronig–Penney problem for equal-height barriers of height $h_0(1-\alpha)$, which is the lowest possible energy configuration for a fixed set of parameters (see Appendix B). These analytical bounds are depicted with respect to α in Fig. 2(f).

The symmetry of the energy spectrum with respect to $\beta = 0.5$ can be explained by noting that the barriers discretely sample the modulation function $h^{\alpha\beta\gamma\Delta}$. When the modulation frequency is larger than the Nyquist frequency $\beta = 0.5$, aliasing occurs since the barriers undersample the modulation signal [30]. This means that frequencies β and $1-\beta$ give identical potential modulation up to a sign.

B. Topological properties

The topological properties of the modulated Kronig–Penney system can be captured by treating each modulation parameter as a quasimomentum of a synthetic dimension. The real-space quasimomentum k and a selected modulation parameter then form a closed torus in parameter space, allowing us to define the Chern number of isolated energy bands. This topological invariant provides information about quantized charge transfer in one dimension and can be related to the conductance of a two-dimensional system [31]. In this section, we look at the different transport regimes hosted by the modulated Kronig–Penney model and how they are related to those observed in the Harper–Hofstadter model. The transported charge is obtained by evaluating the Chern number in two ways: either by directly employing the definition, which requires information about the states, or by using a version of Středa's formula [32], which requires only the knowledge of the energy spectrum, thus allowing faster computation.

The first set of periodic parameters that we consider consists of k and γ. The Chern number associated with the nth sub-band for a selected β value is then calculated as [33]

$$C_n^{(\gamma)} = \frac{1}{2\pi \mathrm{i}} \int_{\mathrm{BZ}} \mathrm{d}k \int_0^{2\pi} \mathrm{d}\gamma\, F_{k\gamma}^{(n)}, \tag{3}$$

where BZ specifies integration over the first Brillouin zone, $F_{k\gamma}^{(n)}$ is the Berry curvature

$$F_{k\gamma}^{(n)} = \frac{\partial}{\partial k}\left\langle u_{k\gamma}^{(n)} \middle| \frac{\partial u_{k\gamma}^{(n)}}{\partial \gamma} \right\rangle - \frac{\partial}{\partial \gamma}\left\langle u_{k\gamma}^{(n)} \middle| \frac{\partial u_{k\gamma}^{(n)}}{\partial k} \right\rangle, \tag{4}$$

and $|u_{k\gamma}^{(n)}\rangle$ are the Bloch eigenstates of the sub-band. The second set of parameters that forms a closed torus in the parameter space is k and Δ, with the Chern number calculated as

$$C_n^{(\Delta)} = \frac{1}{2\pi \mathrm{i}} \int_{\mathrm{BZ}} \mathrm{d}k \int_0^{1} \mathrm{d}\Delta\, F_{k\Delta}^{(n)}. \tag{5}$$

The Chern numbers in each case can be evaluated using Eqs. (3) and (5), however, since the considered model admits a Harper equation representation (see Appendix C), a numerically efficient way to obtain the transported charge is to employ Středa's formula [32,34,35]. The transported charge of the completely occupied sub-bands for the (k, γ) parameter case is then given by

$$C^{(\gamma)} \equiv \sum_{n=1}^{n_{\mathrm{F}}} C_n^{(\gamma)} = \frac{\partial N(E_{\mathrm{F}})}{\partial \beta}, \tag{6}$$

where n_{F} indicates the highest occupied sub-band and $N(E_{\mathrm{F}})$ is the number of states below the Fermi energy E_{F} divided by the total number of states in the band. The total charge transfer $C^{(\gamma)}$ of the lowest energy band is calculated numerically using the finite difference method and shown in Fig. 3(a). The change of $N(E_{\mathrm{F}})$ is divided by the change in modulation frequency of the two closest sampled β points. As long as the given E_{F} remains in the same energy gap between neighboring β, the total charge is obtained accurately; however, due to the finite sampling of β this condition is hard to maintain for small energy gaps. This is especially prevalent for gaps above $E_{K_1}^{\mathrm{mid}}$ as seen in Fig. 3(a), where only the charge transfer of the major gaps can be discerned. Nevertheless, this approach allows us to evaluate the Chern numbers for a large range of β quickly. In contrast, the transferred charge $C^{(\Delta)} \equiv \sum_{n=1}^{n_{\mathrm{F}}} C_n^{(\Delta)}$

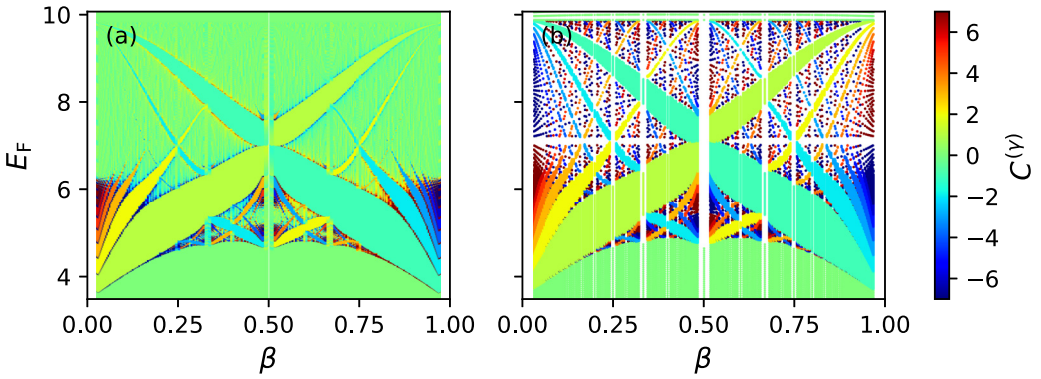

FIG. 3. (a) The total Chern number $C^{(\gamma)}$ represented as an in-gap color, indicating the sum of Chern numbers of the sub-bands below Fermi energy E_F. (b) Same color scale is used to mark t_{n_F} obtained from Diophantine equation (8). The model parameters are $\alpha = 0.5$ and $h_0 = 10$.

in (k, Δ) space is obtained using Eq. (5) and is shown in Fig. 4(a). Integrating the Berry curvature provides more accurate results since the computation is performed for a fixed β, however, numerical errors can still appear when the gap between the energy bands is small and finer parameter discretization is needed.

The two charge-transfer regimes shown in Figs. 3(a) and 4(a) share the same butterfly-like projected bandwidth structure, although their topological properties are different. In particular, the regimes are connected through the Diophantine equation (see Appendix C)

$$pC^{(\gamma)} + qC^{(\Delta)} = n_F, \tag{7}$$

for n_F filled bands. This allows us to establish a connection between the one-dimensional Kronig–Penney model under parameter variation and the charge transfer picture of the two-dimensional lattice with electrons in a magnetic field. Such a system is known as the Hofstadter model, and the information about its transport is encoded in the Diophantine equation of the form

$$pt_{n_F} + qs_{n_F} = n_F, \tag{8}$$

with conditions $2|t_{n_F}| < q$ and $s_{n_F} \in \mathbb{Z}$. It uniquely determines the Hall conductance $\sigma_H^{(n_F)} = \frac{e^2}{2\pi\hbar} t_{n_F}$ of a square lattice pierced by a dimensionless rational magnetic flux $\phi_{\text{flux}} = p/q$ for the system occupied by particles up to the n_Fth energy band [31,36–38]. The integer s_{n_F} is the gap label that fixes the flux-independent part of the integrated density of states $N(E_F)$ once t_{n_F} is determined. It can be interpreted as a Chern number associated with the charge transfer under the translation of the periodic potential [39]. We map the calculated charge t_{n_F} of the Hofstadter model to the energy gaps of the modulated Kronig–Penney model, assuming that $\beta \equiv \phi_{\text{flux}}$. The resulting gap-coloring based on the total Chern number t_{n_F} corresponding to the Hall conductance of the lowest energy band is shown in Fig. 3(b). Comparing it with the charge transfer obtained from Středa's formula at the well-resolved gaps [Fig. 3(a)] we see that the predicted Chern numbers of both models are in good agreement. Comparing $C^{(\Delta)}$ of Fig. 4(a) to s_{n_F} obtained from Eq. (8) and mapped to the gaps of the modulated model [Fig. 4(b)] we get matching Chern numbers up to numerical precision as well.

The origin of the topological similarity between the modulated sub-wavelength-barrier Hamiltonian and the Harper–Hofstadter model lies in the underlying difference equation structure that both models share. The two-dimensional (2D) Harper–Hofstadter lattice model can be mapped to a one-dimensional (1D) Harper equation [40] (also known as the Aubry-André model [41]) by a proper gauge choice [42], while the modulated Kronig–Penney model reduces to a modified Harper equation by employing the Bethe ansatz (see Appendixes B and C). The energy spectra nevertheless differ in detail. In the tight-binding Harper–Hofstadter model, the spectrum is mirrored around zero energy due to the

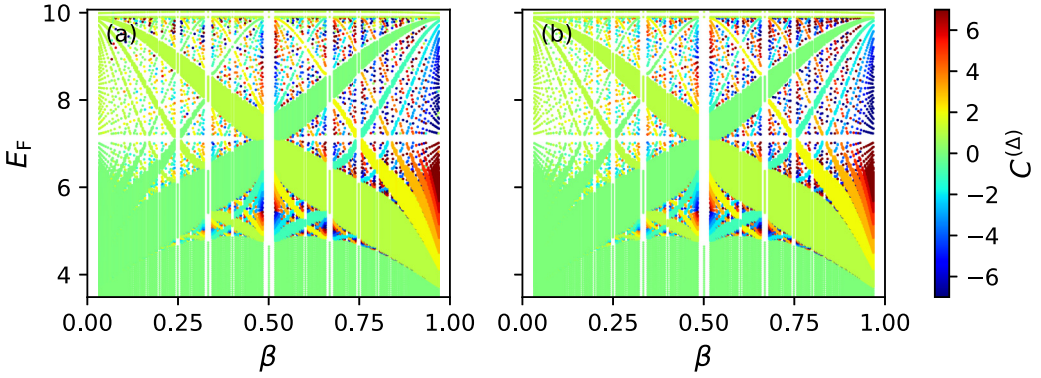

FIG. 4. (a) The total Chern number $C^{(\Delta)}$ as an in-gap color, indicating the sum of Chern numbers $\sum_{n=1}^{n_F} C_n^{(\Delta)}$ of the sub-bands below the Fermi energy E_F. (b) Coloring given by s_{n_F} obtained from Diophantine equation (8). The parameters used are $\alpha = 0.5$ and $h_0 = 10$.

bipartite lattice hopping geometry. By contrast, the modified Harper equation of the continuum Kronig–Penney Hamiltonian breaks this symmetry since energy-dependent on-site terms arise [43], resulting in a butterfly-like dispersion that is generally skewed. Despite these differences, the underlying topological properties are retained as long as the energy gaps do not close.

Two aspects of the modulated Kronig–Penney model go beyond the standard Harper–Hofstadter setting. First, as a continuum system rather than a tight-binding lattice, its spectrum is not bounded from above, providing access to topological structure in higher-energy bands. Second, the model admits an extended modulation parameter space: whereas in the Hofstadter problem the gap-labeling integer s_{n_F} is fixed once the band Hall response is specified, here the associated invariant $C^{(\Delta)}$ is directly accessible experimentally through topological pumps by changing the parameter Δ, as discussed below. Together, these features enable transport responses that differ qualitatively from the canonical lattice case, i.e., filling the entire sub-bands of the lowest band, one can obtain a nontrivial net charge $C^{(\Delta)} = 1$, in contrast with the usual Hofstadter model where filling all the bands yields $C^{(\gamma)} = 0$.

C. Adiabatic transport in real space

The resulting nontrivial topology of the model leads to quantized density charge transfer in real space under the adiabatic change of γ and Δ. This is known as Thouless pumping, which has been observed in a variety of cold atom and condensed-matter systems [17,19,21].

To illustrate transport in our system, we calculate the position expectation value of localized Wannier functions [44] of the occupied bands during a single periodic evolution of the parameters, i.e., a single pumping cycle. For systems with PBC, the position operator $\hat{x}$ is not compatible with translational symmetry on a ring, making its expectation value ill-defined and origin-dependent [45]. A suitable expression that respects the translational symmetry can be constructed using the unitary operator $e^{i\frac{2\pi}{L}\hat{x}}$, defining the position up to modulo of the system length [46],

$$\langle x \rangle = \frac{L}{2\pi} \mathrm{Im}\left[\log\left(\langle e^{i\frac{2\pi}{L}\hat{x}}\rangle\right)\right]. \tag{9}$$

Here L is the length of a ring that consists of M_{cell} elementary cells of length b. Evaluating this expression for the Wannier functions gives the Wannier center position.

We select two modulation frequencies $\beta = 1/3$ and $\beta = 2/3$, which are numerically feasible and capture distinct transport regimes during the variation of γ and Δ, including transport in opposite directions as well as the absence of net transport. We focus on the lowest sub-band of the lowest energy band and assume it is completely filled. The calculated Chern numbers for the considered cases are shown in Table I.The accompanying Fig. 5 illustrates the spatial transport of localized densities for these regimes. The dashed white curves show the instantaneous Wannier centers, which can exhibit small intracell oscillations during the evolution due to the density redistribution as the barrier configuration changes. Only the net displacement after one closed cycle is quantized. In Figs. 5(a) and 5(c), the barriers remain in fixed positions, and the density of Wannier functions $w_0(x)$ is transported across the barriers with the lowest heights while varying γ. The transport in different directions for $\beta = 1/3$ and $\beta = 2/3$ is observed because the modulation envelope is offset by $2\pi/3$ in Fig. 5(a) and $-2\pi/3$ in Fig. 5(c) for each subsequent barrier, leading to the movement of the modulation minima to either right or left during the pump cycle. In Figs. 5(b) and 5(d), the barriers are shifted by Δ in space as well. The Wannier centers are moved through the barriers with the lowest heights, resulting in no net shift after the pumping cycle in Fig. 5(b), whereas in Fig. 5(d) they are transported to the neighboring elementary cell. In all of the cases, the density of a selected Wannier function, after completing a single pumping cycle, gets translated by an integer number of elementary cells. This integer corresponds to the Chern number, with the sign indicating the transport direction as expected (see Table I).

TABLE I. Chern numbers of the first energy band for the parameter spaces (k, γ) and (k, Δ) at selected β. The labels (a)–(d) indicate the matching transport cases of Fig. 5.

	$C_1^{(\gamma)}$	$C_1^{(\Delta)}$
$\beta = 1/3$	1 (a)	0 (b)
$\beta = 2/3$	−1 (c)	1 (d)

In ultracold atom systems, the analyzed transport can be observed using standard techniques such as measuring the center-of-mass movement of an atom cloud under pumping [21]. The Chern number can also be obtained from density-profile measurements [47]. Specifically, for the modulated Kronig–Penney model, it could be done by taking bulk-density snapshots for different values of the modulation

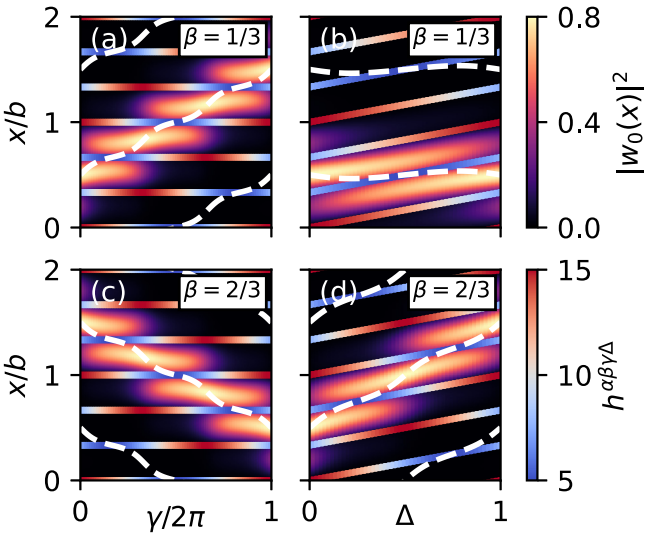

FIG. 5. Spatial transfer of localized Wannier function density $|w_0(x)|^2$ under adiabatic change of γ and Δ when the lowest-energy sub-band is filled for modulation $\beta = 1/3$ in panels (a) and (b) and $\beta = 2/3$ in panels (c) and (d). Two elementary cells are shown with barrier positions and heights indicated by $h^{\alpha\beta\gamma\Delta}$. The dashed white curves are position expectation values of Wannier functions of neighboring elementary cells.

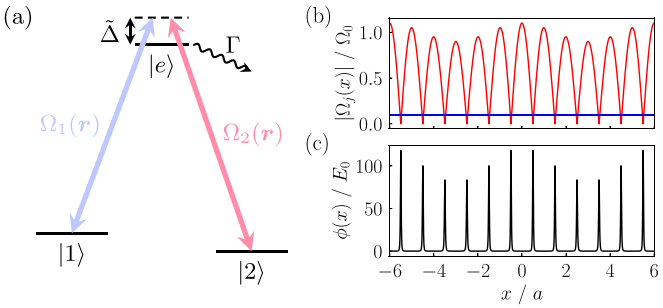

FIG. 6. (a) Lambda atom-light coupling configuration for ultracold atoms. (b) Spatial dependence of the modulus of Rabi frequencies Ω_1 and Ω_2 obtained from Eqs. (14)–(17) for $\epsilon = 0.1$, $\alpha = 0.1$, $\beta = 1/3$, $\gamma = 0$, $k = 1$, $\theta = 0$. (c) Position dependence of geometric scalar potential ϕ for aforementioned Ω_j configuration, obtained from Eq. (13) for the same parameters.

frequency and extracting the topological invariant from the resulting density change, in direct analogy to Středa-type protocols based on magnetic flux variation in the Harper–Hofstadter model [48].

D. Experimental realization

Let us also propose a concrete experimental scheme to realize the aforementioned Kronig–Penney-type model. For this, we consider ultracold atoms in a Λ configuration with two ground states $|1\rangle$ and $|2\rangle$ and an excited state $|e\rangle$, as depicted in Fig. 6(a). In general, the excited state experiences spontaneous emission, characterized by the decay rate Γ. The low-lying states $|1\rangle$ and $|2\rangle$ are off-resonantly coupled (with detuning $\tilde{\Delta}$) to the excited state $|e\rangle$ by laser fields, which are characterized by spatially dependent Rabi frequencies $\Omega_1(\mathbf{r})$ and $\Omega_2(\mathbf{r})$, respectively. In what follows, we usually keep the position dependence implicit.

Applying the rotating wave approximation [49], the standard atom-light coupling Hamiltonian can be written as

$$\hat{V}/\hbar = \sum_{j=1}^{2}\left(\frac{\Omega_j}{2}|e\rangle\langle j| + \text{H.c.}\right) - \left(\tilde{\Delta} + \frac{\mathrm{i}}{2}\Gamma\right)|e\rangle\langle e|, \quad (10)$$

which supports a dark state solution with eigenvalue 0, which is given by [50,51]

$$|D\rangle = \frac{1}{\Omega}(\Omega_2|1\rangle - \Omega_1|2\rangle), \quad (11)$$

where $\Omega = (|\Omega_1|^2 + |\Omega_2|^2)^{1/2}$.

When the amplitude of the Rabi frequencies is much larger than the characteristic kinetic energy, the atoms adiabatically follow the dark state, i.e., $|\psi(\mathbf{r})\rangle \approx \psi_D(\mathbf{r})\,|D(\mathbf{r})\rangle$ [50,52–54]. Then, the dark state wave function ψ_D is governed by the dark state Hamiltonian

$$\hat{H}_\mathrm{D} = -\frac{\mathrm{d}^2}{\mathrm{d}x^2} + \phi, \quad (12)$$

where ϕ is the geometric scalar potential [52,54]

$$\phi = \frac{\nabla\zeta^* \cdot \nabla\zeta}{(1+|\zeta|^2)^2}, \quad (13)$$

and $\zeta = \Omega_1/\Omega_2$ is the Rabi frequency ratio. Note that, for a one-dimensional system, the vector potential can always be gauged away and, thus, is not shown. Henceforth, we take the Rabi frequencies to be purely real.

Looking at Eq. (13), we see that the amplitude of the scalar potential depends on the spatial variation of the Rabi frequency ratio. Consequently, a sub-wavelength Kronig–Penney lattice can be engineered if one of the Rabi frequencies periodically goes to zero, while the other has a much smaller constant amplitude [6,9]. To additionally obtain modulated Dirac-δ scatterer heights, one may add an amplitude envelope on one (or both) of the Rabi frequencies.

More concretely, consider the following class of configurations:

$$\Omega_1(x) = \Omega_0 f_1(x)\sin(kx+\theta), \quad (14)$$

$$\Omega_2(x) = \epsilon\Omega_0 f_2(x), \quad (15)$$

where Ω_0 is the Rabi frequency amplitude, ϵ is the amplitude ratio, k is the wave vector, θ is the spatial phase, and $f_i(x)$ are functions of order unity with no real roots ($i \in \{1,2\}$).

Then consider the vicinity of a zero of $\Omega_1(x)$ at $x = x_j$. One can show that the geometric scalar potential approaches a Dirac-δ peak at $x = x_j$ with amplitude $\pi\delta(x-x_j)/2\epsilon_j$ as $\epsilon \to 0$, where $\epsilon_j = \epsilon f_2(x_j)/f_1(x_j)$ [4]. Since $\Omega_1(x)$ is periodic, one obtains a sub-wavelength-barrier array with a spatial period $a = \pi/k$.

To obtain the considered Kronig–Penney lattice, given by Eq. (1), one can take the following envelope functions:

$$f_1(x) = h^{\alpha\beta\gamma\Delta}(x)/h_0, \quad f_2(x) = 1, \quad (16)$$

where

$$h^{\alpha\beta\gamma\Delta}(x) = h_0[1+\alpha\cos(2\pi\beta x^\Delta - \gamma)], \quad (17)$$

and $x^\Delta = x + \Delta$. Of course, one has $h^{\alpha\beta\gamma\Delta}(x_j) = h_j^{\alpha\beta\gamma\Delta}$.

For clarity, the Rabi frequencies and the resulting geometric scalar potential are shown in Figs. 6(b) and 6(c), respectively. Note that in principle, there are many possible configurations to achieve the desired lattice since the Dirac-δ amplitude is determined only by the envelope function ratio at $x = x_j$ and not the individual envelope function values.

IV. SUMMARY AND OUTLOOK

In this work, we have demonstrated that a spatially modulated sub-wavelength-barrier lattice exhibits nontrivial band topology characteristic of Hofstadter-type systems. The modulation of the barrier strengths fragments the bands into multiple sub-bands and produces a Hofstadter-butterfly-like spectrum with analytically controllable bounds. Treating the modulation parameters as synthetic dimensions, we identified two pumping geometries, (k,γ) and (k,Δ), which display distinct quantized transport regimes under adiabatic variation. The associated Chern numbers, obtained from the Berry curvature and a Středa-type relation, are linked by a Harper–Hofstadter-like Diophantine equation, providing a connection between the modulated continuum model and the quantum Hall lattice problem. These bulk invariants are directly reflected in real-space Thouless pumping, where Wannier

centers shift by an integer number of elementary cells over a pumping cycle.

We have also outlined a concrete implementation based on dark-state optical potentials in a three-level Λ configuration, where position-dependent Rabi frequencies generate an array of modulated Dirac-δ barriers. Such setups are compatible with current ultracold atomic gas experiments, making modulated Kronig–Penney systems a practical platform for realizing Hofstadter-type topology in reduced dimensionality. While our analysis focused on bulk properties, the flexibility in engineering barrier configurations and band topologies suggests straightforward extensions to topological interfaces and edge-state physics. In future work, it will be of particular interest to investigate how interactions and disorder modify the topological transport identified here, and to develop controlled nonadiabatic driving protocols for manipulating transport beyond the strictly adiabatic regime.

ACKNOWLEDGMENTS

This work was supported by the Okinawa Institute of Science and Technology Graduate University (OIST) and utilized the computing resources of the Scientific Computing and Data Analysis section of Core Facilities at OIST. This work was initiated by a SHINKA grant, a joint grant between OIST and Tohoku University, and supported by the JSPS Bilateral Program No. JPJSBP120244202. D.B. is supported by the Research Council of Lithuania (RCL) Grant No. S-LJB-24-2 and the JSPS Bilateral Program No. JPJSBP120244202. This work has also received funding from COST Action POLYTOPO CA23134, supported by COST (European Cooperation in Science and Technology). T.O. is supported by JSPS KAKENHI Grant No. JP24K00548 and JST PRESTO Grant No. JPMJPR2353.

DATA AVAILABILITY

The data that support the findings of this article are not publicly available upon publication because it is not technically feasible and/or the cost of preparing, depositing, and hosting the data would be prohibitive within the terms of this research project. The data are available from the authors upon reasonable request.

APPENDIX A: HAMILTONIAN MATRIX ELEMENTS OF PERIODIC BOUNDARY MODULATED KRONIG-PENNEY MODEL

Let the height modulation frequency in Eq. (1) be rational, i.e., $\beta = \frac{p}{q}$ where p and q are coprime integers. In this case, for a given β, an elementary supercell of length b exists. To solve the eigenvalue problem, we use Bloch's theorem, stating that the eigenfunctions of a periodic system have the form $\psi_k^{(n)}(x) = \mathrm{e}^{\mathrm{i}kx}u_k^{(n)}(x)$. Here n is the quantum number labeling the energy bands, $u_k^{(n)}(x) = u_k^{(n)}(x+b)$ is the periodic part of the Bloch wave function, and k is the quasimomentum. If periodic boundary conditions are imposed, the quasimomentum takes discrete values $k = \frac{2\pi\ell}{M_{\mathrm{cell}}b}$ with $\ell \in \{-\frac{M_{\mathrm{cell}}}{2}, \frac{M_{\mathrm{cell}}}{2}+1, \ldots, \frac{M_{\mathrm{cell}}}{2}-1\}$, with M_{cell} being the number of supercells. In the infinite-lattice case k is continuous. Acting with the model Hamiltonian on the wave function ansatz, we get a set of decoupled equations for each k with the periodic part of the wave function as the eigensolution:

$$\left[\left(\mathrm{i}\frac{\mathrm{d}}{\mathrm{d}x} - k\right)^2 + V(x)\right]u_k^{(n)}(x) = E_n u_k^{(n)}(x), \tag{A1}$$

with $V(x) = \sum_{j\in\mathcal{M}} h_j^{\alpha\beta\gamma\Delta}\delta(x - x_j^{\Delta})$ and energy eigenvalues E_n. We can write the matrix representation of this Hamiltonian in the plane-wave basis $\phi_m(x) = \frac{1}{\sqrt{b}}\mathrm{e}^{\mathrm{i}\frac{2\pi m}{b}x}$, $m \in \mathbb{Z}$. The solutions are then $u_k^{(n)}(x) = \sum_{m=-\infty}^{\infty} c_{mk}^{(n)}\phi_m(x)$, with coefficients $c_{mk}^{(n)} \in \mathbb{C}$ obtained by diagonalizing the Hamiltonian matrix. The explicit form of the matrix elements is

$$H_{ml} \equiv \int_0^b \mathrm{d}x\, \phi_m^*(x) H \phi_l(x) = \left(k + \frac{2\pi l}{b}\right)^2 \delta_{ml} + \frac{1}{b}\sum_{j\in\mathcal{M}_{\mathrm{cell}}} h_j^{\alpha\beta\gamma\Delta}\mathrm{e}^{\mathrm{i}\frac{2\pi(l-m)}{b}x_j^{\Delta}}, \tag{A2}$$

where the sum is over the set $\mathcal{M}_{\mathrm{cell}}$ of barriers indexed in a single supercell.

For numerical calculations, the plane-wave number cutoff is $|m_{\mathrm{cutoff}}| = 1000$ modes. The dispersions $E(k,\gamma)$ and $E(k,\Delta)$, for fixed α and β, are computed by discretizing the parameter ranges $k \in [-\frac{\pi}{b}, \frac{\pi}{b})$, $\gamma \in [0, 2\pi)$, and $\Delta \in [0, 1)$ into 50 evenly spaced points. The bandwidths of both dispersion spectra coincide, and the energy-band projections for each β are shown for the two lowest bands in Fig. 7. The second band retains the features of the first band, but the fractalization of the gaps is less pronounced.

APPENDIX B: DETERMINING ANALYTICAL LIMITS OF THE MODULATED KRONIG–PENNEY MODEL

We start with the Hamiltonian (1) of the main text,

$$H = -\frac{\mathrm{d}^2}{\mathrm{d}x^2} + \sum_{j\in\mathcal{M}} h_j\delta(x - x_j), \tag{B1}$$

where we have dropped the indices indicating parameter dependence for brevity. We assume that the wave function between the barriers supports a piece-wise plane-wave solution, i.e.,

$$\psi(x) = A_j\mathrm{e}^{\mathrm{i}\sqrt{E}x} + B_j\mathrm{e}^{-\mathrm{i}\sqrt{E}x} \text{ for } x_{j-1} < x \leqslant x_j, \quad j \in \mathcal{M}, \tag{B2}$$

given the eigenproblem $H\psi(x) = E\psi(x)$. At the position of the jth barrier, we use the continuity of the wave function

$$\lim_{\varepsilon\to 0}[\psi(x_j + \varepsilon) - \psi(x_j - \varepsilon)] = 0, \tag{B3}$$

which leads to the following condition for the first derivative:

$$\lim_{\varepsilon\to 0}\left[\left.\frac{\mathrm{d}\psi(x)}{\mathrm{d}x}\right|_{x_j+\varepsilon} - \left.\frac{\mathrm{d}\psi(x)}{\mathrm{d}x}\right|_{x_j-\varepsilon}\right] = h_j\psi(x_j). \tag{B4}$$

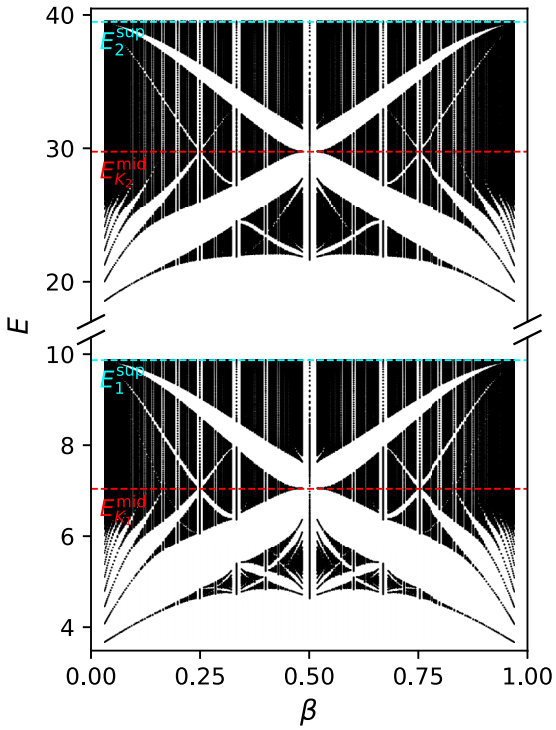

FIG. 7. Splitting of the two lowest-energy bands $E(\beta)$ under the change of modulation frequency for $h_0 = 10$, $\alpha = 0.5$, $\Delta = 0$. The dependence on k and γ is projected onto the energy axis for each β. The number of elementary cells is taken to be $\mathcal{M}_{\text{cell}} = 50$. The cyan dashed line indicates the upper bound of the energy E_j^{sup}, and the red dashed line indicates the standing-wave solution energy $E_{K_j}^{\text{mid}}$ for each band $j \in \{1, 2\}$.

Using these relations, one arrives at the relations of coefficients between neighboring regions

$$\tilde{A}_{j+1}e^{-i\sqrt{E}a} = \left(1 - \frac{ih_j}{2\sqrt{E}}\right)\tilde{A}_j - \frac{ih_j}{2\sqrt{E}}\tilde{B}_j,$$
$$\tilde{B}_{j+1}e^{i\sqrt{E}a} = \frac{ih_j}{2\sqrt{E}}\tilde{A}_j + \left(1 + \frac{ih_j}{2\sqrt{E}}\right)\tilde{B}_j. \quad \text{(B5)}$$

Here, $\tilde{A}_j \equiv A_j e^{i\sqrt{E}x_j}$, $\tilde{B}_j \equiv B_j e^{-i\sqrt{E}x_j}$, and a is the separation between nearest barriers. Noting that $\psi_j \equiv \psi(x_j) = \tilde{A}_j + \tilde{B}_j$, Eqs. (B5) can be expressed as

$$\frac{1}{2}(\psi_{j+1} + \psi_{j-1}) - \frac{h_j \sin(\sqrt{E}a)}{2\sqrt{E}}\psi_j = \cos(\sqrt{E}a)\psi_j. \quad \text{(B6)}$$

A feature of the butterfly-like spectrum can be immediately inferred where the barriers are equal for a given β during parameter change. This corresponds to the formation of standing waves with zero group velocity, i.e., $\frac{1}{2}(\psi_{j+1} + \psi_{j-1}) = 0$, which leads to the condition $\frac{h\sin(\sqrt{E_n}a)}{2\sqrt{E_n}} + \cos(\sqrt{E_n}a) = 0$ for the nth band, when all barrier heights are equal to h. The energy solutions correspond to $E_n \propto E_{K_n}^{\text{mid}}$ in the main text. One can also recover the standard Kronig–Penney result by Fourier expanding the coefficients $\psi_j = \sum_k e^{ikx_j}\psi_k$, leading to

$$\cos(ka) - \frac{h\sin(\sqrt{E}a)}{2\sqrt{E}} = \cos(\sqrt{E}a). \quad \text{(B7)}$$

Setting the quasimomentum value $k = 0$ and solving the equation allows us to find the lower bound E_1^{inf} of the energy spectrum for the butterfly-like structure.

APPENDIX C: RELATION TO HARPER–HOFSTADTER EQUATION

The modulated Kronig–Penney Eq. (B6) derived in the previous section can be rewritten as

$$\psi_{j+1} + \psi_{j-1} + g_1(E)\cos(2\pi\beta x_j - \varphi)\psi_j = g_2(E)\psi_j, \quad \text{(C1)}$$

where we have denoted the modulation phase as

$$\varphi = \gamma - 2\pi\beta\Delta, \quad \text{(C2)}$$

and the energy-dependent terms by

$$g_1(E) \equiv -\frac{\alpha h_0 \sin(\sqrt{E}a)}{\sqrt{E}}, \quad \text{(C3)}$$
$$g_2(E) \equiv 2\cos(\sqrt{E}a) + \frac{h_0 \sin(\sqrt{E}a)}{\sqrt{E}}. \quad \text{(C4)}$$

The obtained Eq. (C1) shares the discrete difference equation structure of the Harper–Hofstadter model with an energy-dependent modulation coefficient. The modulation frequency β plays an analogous role to the dimensionless magnetic flux ϕ_{flux} in the 2D Hofstadter model written in the Harper equation form [39]. A Thouless pump cycle in the Harper equation is realized by adiabatically changing the phase parameter φ from 0 to 2π. The charge transported during such a period for a selected n band is equal to the Chern number

$$C_n^{(\varphi)} = \frac{1}{2\pi i}\int_{\text{BZ}} dk \int_0^{2\pi} d\varphi\, F_{k\varphi}^{(n)}, \quad \text{(C5)}$$

where the superscript indicates the pumping parameter considered. We immediately see that when Δ is fixed and the pumping is induced by changing γ, the pumped charge precisely coincides with the Hofstadter-model case, i.e., $C_n^{(\gamma)} = C_n^{(\varphi)}$. It is known that, for n_F occupied energy sub-bands of the Hofstadter model, the transported charge can be related by the Středa-Widom formula

$$\frac{e^2}{2\pi\hbar}\sum_{n=1}^{n_{\text{F}}} C_n^{(\varphi)} = e\frac{\partial\rho(E_{\text{F}})}{\partial B}, \quad \text{(C6)}$$

where e is the electron charge, B is the magnetic field, and $\rho(E_{\text{F}}) = \frac{N(E_{\text{F}})}{A_{\text{cell}}}$ is the particle density with A_{cell} being the elementary cell area and $N(E_{\text{F}})$ the density of occupied states per band, given that all energy levels below E_{F} are filled. Expressing the equation in terms of dimensionless magnetic flux $\phi_{\text{flux}} = cBA_{\text{cell}}/2\pi\hbar$, we get

$$C^{(\varphi)} \equiv \sum_{n=1}^{n_{\text{F}}} C_n^{(\varphi)} = \frac{\partial N(E_{\text{F}})}{\partial\phi_{\text{flux}}}. \quad \text{(C7)}$$

An analogous relation is valid for the Kronig–Penney model if the dimensionless flux is replaced by the spatial modulation frequency of the barriers, provided that the functions $g_1(E)$ and $g_2(E)$ only smoothly deform the energy bands without

closing the gap

$$C^{(\gamma)} = \frac{\partial N(E_{\mathrm{F}})}{\partial \beta}. \tag{C8}$$

This is Eq. (6) used in the main text.

If γ is fixed and Δ is varied, the Chern number for a single pump cycle is

$$C_n^{(\Delta)} = \frac{1}{2\pi \mathrm{i}} \int_{\mathrm{BZ}} \mathrm{d}k \int_0^1 \mathrm{d}\Delta \, F_{k\Delta}^{(n)}. \tag{C9}$$

For rational modulation $\beta = p/q$, the transported charge $C^{(\Delta)}$ can be related to $C^{(\gamma)}$ by noting that performing the Δ pump cycle q times shifts the phase φ by $-2\pi p$ and the barriers are shifted by an elementary lattice cell. Shifting the barriers transports n_{F} charges corresponding to the filled number of sub-bands [17], and the phase change contributes $-pC^{(\gamma)}$, leading to the total charge transport

$$qC^{(\Delta)} = n_{\mathrm{F}} - pC^{(\gamma)}. \tag{C10}$$

Rearranging gives the Diophantine equation for the considered modulated Kronig–Penney model

$$pC^{(\gamma)} + qC^{(\Delta)} = n_{\mathrm{F}}, \tag{C11}$$

or alternatively

$$C^{(\Delta)} + \beta C^{(\gamma)} = N(E_{\mathrm{F}}), \tag{C12}$$

which can also be obtained by integrating Středa's equation (6).

[1] K. R. De L. and P. W. George, Quantum mechanics of electrons in crystal lattices, Proc. R. Soc. London A **130**, 499 (1931).

[2] A. Sánchez, E. Maciá, and F. Domínguez-Adame, Suppression of localization in Kronig-Penney models with correlated disorder, Phys. Rev. B **49**, 147 (1994).

[3] S. Vaidya, C. Jörg, K. Linn, M. Goh, and M. C. Rechtsman, Reentrant delocalization transition in one-dimensional photonic quasicrystals, Phys. Rev. Res. **5**, 033170 (2023).

[4] M. Łącki and J. Zakrzewski, Random Kronig-Penney-type potentials for ultracold atoms using dark states, Phys. Rev. A **108**, 053326 (2023).

[5] F. M. Izrailev, A. A. Krokhin, and N. M. Makarov, Anomalous localization in low-dimensional systems with correlated disorder, Phys. Rep. **512**, 125 (2012).

[6] M. Łącki, M. A. Baranov, H. Pichler, and P. Zoller, Nanoscale "dark state" optical potentials for cold atoms, Phys. Rev. Lett. **117**, 233001 (2016).

[7] Y. Wang, S. Subhankar, P. Bienias, M. Lacki, T.-C. Tsui, M. A. Baranov, A. V. Gorshkov, P. Zoller, J. V. Porto, and S. L. Rolston, Dark state optical lattice with a subwavelength spatial structure, Phys. Rev. Lett. **120**, 083601 (2018).

[8] M. Lacki, P. Zoller, and M. A. Baranov, Stroboscopic painting of optical potentials for atoms with subwavelength resolution, Phys. Rev. A **100**, 033610 (2019).

[9] E. Gvozdiovas, P. Račkauskas, and G. Juzeliūnas, Optical lattice with spin-dependent sub-wavelength barriers, SciPost Phys. **11**, 100 (2021).

[10] E. Gvozdiovas, I. B. Spielman, and G. Juzeliūnas, Interference-induced anisotropy in a two-dimensional dark-state optical lattice, Phys. Rev. A **107**, 033328 (2023).

[11] G. Ritt, C. Geckeler, T. Salger, G. Cennini, and M. Weitz, Fourier synthesis of optical potentials for atomic quantum gases, Phys. Rev. A **74**, 063622 (2006).

[12] N. Lundblad, P. J. Lee, I. B. Spielman, B. L. Brown, W. D. Phillips, and J. V. Porto, Atoms in a radio-frequency-dressed optical lattice, Phys. Rev. Lett. **100**, 150401 (2008).

[13] A. González-Tudela, C.-L. Hung, D. E. Chang, J. I. Cirac, and H. J. Kimble, Subwavelength vacuum lattices and atom–atom interactions in two-dimensional photonic crystals, Nat. Photonics **9**, 320 (2015).

[14] U. Kuhl and H.-J. Stöckmann, Microwave realization of the Hofstadter butterfly, Phys. Rev. Lett. **80**, 3232 (1998).

[15] S. Mishra and S. Satpathy, One-dimensional photonic crystal: The Kronig-Penney model, Phys. Rev. B **68**, 045121 (2003).

[16] K. v. Klitzing, G. Dorda, and M. Pepper, New method for high-accuracy determination of the fine-structure constant based on quantized Hall resistance, Phys. Rev. Lett. **45**, 494 (1980).

[17] D. J. Thouless, Quantization of particle transport, Phys. Rev. B **27**, 6083 (1983).

[18] T. Ozawa, H. M. Price, A. Amo, N. Goldman, M. Hafezi, L. Lu, M. C. Rechtsman, D. Schuster, J. Simon, O. Zilberberg, and I. Carusotto, Topological photonics, Rev. Mod. Phys. **91**, 015006 (2019).

[19] R. Citro and M. Aidelsburger, Thouless pumping and topology, Nat. Rev. Phys. **5**, 87 (2023).

[20] L. Wang, M. Troyer, and X. Dai, Topological charge pumping in a one-dimensional optical lattice, Phys. Rev. Lett. **111**, 026802 (2013).

[21] S. Nakajima, T. Tomita, S. Taie, T. Ichinose, H. Ozawa, L. Wang, M. Troyer, and Y. Takahashi, Topological thouless pumping of ultracold fermions, Nat. Phys. **12**, 296 (2016).

[22] M. Lohse, C. Schweizer, O. Zilberberg, M. Aidelsburger, and I. Bloch, A Thouless quantum pump with ultracold bosonic atoms in an optical superlattice, Nat. Phys. **12**, 350 (2016).

[23] Y. E. Kraus, Y. Lahini, Z. Ringel, M. Verbin, and O. Zilberberg, Topological states and adiabatic pumping in quasicrystals, Phys. Rev. Lett. **109**, 106402 (2012).

[24] I. Reshodko, A. Benseny, J. Romhányi, and T. Busch, Topological states in the Kronig–Penney model with arbitrary scattering potentials, New J. Phys. **21**, 013010 (2019).

[25] T. B. Smith and A. Principi, A bipartite Kronig–Penney model with Dirac-delta potential scatterers, J. Phys.: Condens. Matter **32**, 055502 (2020).

[26] W.-B. He, G. Žlabys, H. Hiyane, S. Sasidharan Nair, and T. Busch, Lieb excitations and topological flat mode of the spectral function of a Tonks-Girardeau gas in a Kronig-Penney potential, Phys. Rev. A **111**, 013312 (2025).

[27] S. S. Nair, G. Žlabys, W.-B. He, T. Fogarty, and T. Busch, Quench dynamics in topologically nontrivial quantum many-body systems, Phys. Rev. A **111**, 033313 (2025).

[28] D. R. Hofstadter, Energy levels and wave functions of Bloch electrons in rational and irrational magnetic fields, Phys. Rev. B **14**, 2239 (1976).

[29] Y. Hasegawa, Y. Hatsugai, M. Kohmoto, and G. Montambaux, Stabilization of flux states on two-dimensional lattices, Phys. Rev. B **41**, 9174 (1990).

[30] C. E. Shannon, Communication in the presence of noise, Proc. IRE **37**, 10 (2006).

[31] D. J. Thouless, M. Kohmoto, M. P. Nightingale, and M. den Nijs, Quantized Hall conductance in a two-dimensional periodic potential, Phys. Rev. Lett. **49**, 405 (1982).

[32] P. Streda, Theory of quantised Hall conductivity in two dimensions, J. Phys. C: Solid State Phys. **15**, L717 (1982).

[33] T. Fukui, Y. Hatsugai, and H. Suzuki, Chern numbers in discretized Brillouin zone: Efficient method of computing (spin) Hall conductances, J. Phys. Soc. Jpn. **74**, 1674 (2005).

[34] R. O. Umucalılar, H. Zhai, and M. Ö. Oktel, Trapped Fermi gases in rotating optical lattices: Realization and detection of the topological Hofstadter insulator, Phys. Rev. Lett. **100**, 070402 (2008).

[35] F. Yılmaz, F. N. Ünal, and M. Ö. Oktel, Evolution of the Hofstadter butterfly in a tunable optical lattice, Phys. Rev. A **91**, 063628 (2015).

[36] G. H. Wannier, A result not dependent on rationality for Bloch electrons in a magnetic field, Phys. Status Solidi B **88**, 757 (1978).

[37] A. H. MacDonald, Landau-level subband structure of electrons on a square lattice, Phys. Rev. B **28**, 6713 (1983).

[38] I. Dana, Y. Avron, and J. Zak, Quantised Hall conductance in a perfect crystal, J. Phys. C: Solid State Phys. **18**, L679 (1985).

[39] M. Kohmoto, Flux and the quantized Hall conductance in two-dimensional periodic systems, J. Phys. Soc. Jpn. **61**, 2645 (1992).

[40] P. G. Harper, Single band motion of conduction electrons in a uniform magnetic field, Proc. Phys. Soc. London Sect. A **68**, 874 (1955).

[41] S. Aubry and G. André, Analyticity breaking and Anderson localization in incommensurate lattices, Ann. Israel Phys. Soc. **3**, 133 (1980).

[42] Y. E. Kraus and O. Zilberberg, Topological equivalence between the Fibonacci quasicrystal and the Harper model, Phys. Rev. Lett. **109**, 116404 (2012).

[43] J. B. Sokoloff, Unusual band structure, wave functions and electrical conductance in crystals with incommensurate periodic potentials, Phys. Rep. **126**, 189 (1985).

[44] N. Marzari, A. A. Mostofi, J. R. Yates, I. Souza, and D. Vanderbilt, Maximally localized Wannier functions: Theory and applications, Rev. Mod. Phys. **84**, 1419 (2012).

[45] R. Resta, Quantum-mechanical position operator in extended systems, Phys. Rev. Lett. **80**, 1800 (1998).

[46] J. K. Asbóth, L. Oroszlány, and A. Pályi, *A Short Course on Topological Insulators* (Springer International Publishing, Cham, 2016).

[47] C. Repellin, J. Léonard, and N. Goldman, Fractional Chern insulators of few bosons in a box: Hall plateaus from center-of-mass drifts and density profiles, Phys. Rev. A **102**, 063316 (2020).

[48] J. Léonard, S. Kim, J. Kwan, P. Segura, F. Grusdt, C. Repellin, N. Goldman, and M. Greiner, Realization of a fractional quantum Hall state with ultracold atoms, Nature (London) **619**, 495 (2023).

[49] M. O. Scully and M. S. Zubairy, *Quantum Optics* (Cambridge University Press, Cambridge, 1997).

[50] J. Dalibard, F. Gerbier, G. Juzeliūnas, and P. Öhberg, *Colloquium*: Artificial gauge potentials for neutral atoms, Rev. Mod. Phys. **83**, 1523 (2011).

[51] J. R. Morris and B. W. Shore, Reduction of degenerate two-level excitation to independent two-state systems, Phys. Rev. A **27**, 906 (1983).

[52] G. Juzeliūnas, P. Öhberg, J. Ruseckas, and A. Klein, Effective magnetic fields in degenerate atomic gases induced by light beams with orbital angular momenta, Phys. Rev. A **71**, 053614 (2005).

[53] N. Goldman, G. Juzeliūnas, P. Öhberg, and I. B. Spielman, Light-induced gauge fields for ultracold atoms, Rep. Prog. Phys. **77**, 126401 (2014).

[54] G. Juzeliūnas, J. Ruseckas, and P. Öhberg, Effective magnetic fields induced by EIT in ultra-cold atomic gases, J. Phys. B: At. Mol. Opt. Phys. **38**, 4171 (2005).